31st Congress of the International Council of the Aeronautical Sciences

Belo Horizonte, Brazil; September 09-14, 2018

MULTI-VARIABLE AIRCRAFT DIRECTIONAL CONTROL WITH ANTI-SKID DIFFERENTIAL BRAKES

Gianpietro Di Rito*, Roberto Galatolo*, Francesco Schettini *

***Università di Pisa - Dipartimento di Ingegneria Civile ed Industriale**
Largo Lucio Lazzarino 2, 56122, Pisa – Italia

Keywords: *runway dynamics, fault-tolerant control, hydraulic brakes, more-electric systems*

Abstract

The paper deals with the design of a fault-tolerant control system of the runway dynamics for small jet aircrafts, in which hydraulic differential brakes are used as a stand-by directional command, to be activated in case of electro-mechanical nose-wheel steering failure. The directional control system is composed of four nested feedback loops, respectively acting on the brake pressures, the wheels' slip ratio, the aircraft heading and the ground path. The study, performed by integrating detailed models of hydraulic brakes and electro-mechanical nose-wheel steering in a light jet aircraft simulator, aims at demonstrating that, in case of nose-wheel steering jamming, the redundant control architecture is capable to assure safe and satisfactory operations, but only if the differential brakes are activated with minimum fault detection latency. Simulation results allow highlighting and characterizing, at different runway conditions, the effects of jamming detection latency on the directional stability when the aircraft crosses severe lateral gusts.

1 Introduction

Although the "more-electric" concept is continuously granting interest in the aerospace sector, the applicability of Electro-Mechanical Actuators (EMAs) in civil transport airliners, well proved in terms of load and speed performances [1][2][3][4], still entails several concerns in terms of safety and reliability. For these aircraft categories, EMAs are often avoided for safety-critical functions (primary flight controls, brakes, landing gears, nose wheel steering), essentially because the statistical database on EMA components' fault modes is poor [5][6][7]. In aerospace EMAs, the electrical faults are typically not an issue, because they can be counteracted by using redundant architectures [8][9][10][11][12][13]. On the other hand, the mechanical faults are more problematic, and the transmission jamming is surely the most critical condition. The EMA jamming occurs because the load is transmitted through mechanical contacts with high local stresses, which cause fatigue in the materials. The degradation of the contact surfaces initially implies lower efficiency (with impact on power consumption [14]) and increased freeplay (with possible impact on aeroservoelastic stability in flight control applications [15][16]). As a final effect, the degradation can lead to a mechanical block. Several EMA components can cause a jamming: gear trains and screw-nut assemblies, primary bearings supporting the actuator loads, secondary bearings included in the motor and the reducer. The jamming of a safety-critical actuator can represent a failure with catastrophic consequences, which makes useless any architecture based on either parallel or grouped actuators. Many research efforts have been and are made to neutralize the problem, with two main approaches:

- to minimize the fault effect, by isolating the jamming inside the EMA (e.g. by adding redundant mechanical channels or by integrating unlock devices);
- to avoid the fault, by anticipating the jamming with Prognostic Health-Management (PHM) algorithms .

In any case, the (potentially) severe consequences related to a jammed EMA require to verify the systems robustness in case of uncompensated fault, and to implement compensation strategies for minimizing the fault effect at aircraft level.

Starting from these considerations, the work proposes the design of a fault-tolerant control system of the runway dynamics for small jet aircrafts, in which hydraulic differential brakes are used as a stand-by directional command, to be activated in case of electro-mechanical nose-wheel steering failure. The study aims at demonstrating that, in case of nose-wheel steering jamming, the redundant control architecture is capable to assure safe and satisfactory operations, but only if the differential brakes are activated with minimum fault detection latency. To perform the analysis, detailed models of hydraulic brake actuators and nose-wheel steering EMA have been integrated in a light jet aircraft simulator, and an extensive simulation campaign has been carried out for highlighting and characterizing, at different runway conditions, the effects of jamming detection latency on the directional stability when the aircraft crosses severe lateral gusts. The models of the 6-dof aircraft dynamics, hydraulic brakes, nose-wheel steering EMA, aerodynamic loads and tyre loads have been entirely developed starting from physical first principles, and implemented in the Matlab-Simulink environment.

2 System Description

2.1 Reference aircraft

A light business jet has been selected as reference aircraft for the study [17], Fig. 1. This choice derives from the growing interest of the aerospace world on the expansion of Small Air Transport (SAT), which is currently viewed as a strategic sector for new aircrafts' development [18]. In this perspective, system design solutions targeting the reliability and safety enhancement could speed up the SAT diffusion.

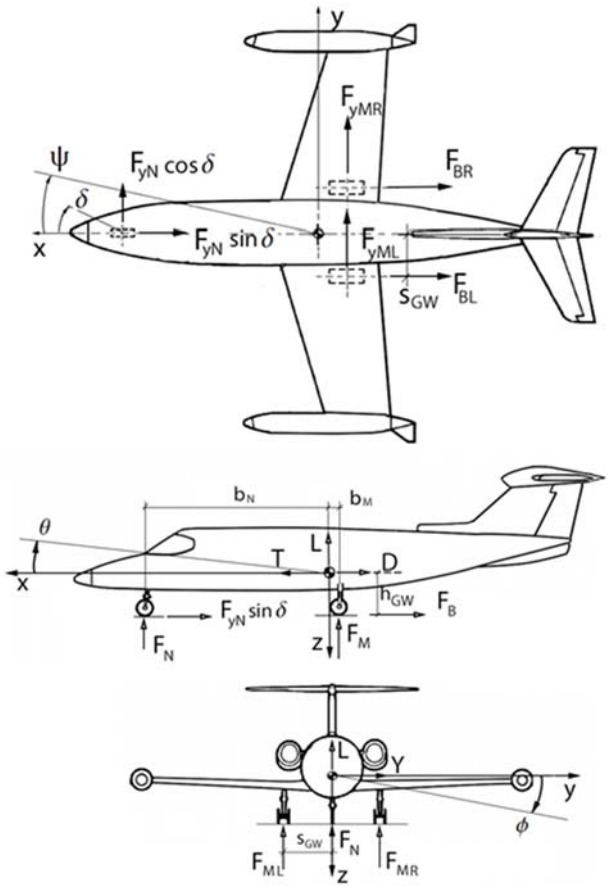

Fig. 1. Reference aircraft [17].

2.2 Fault-tolerant directional control system

The proposed fault-tolerant directional control system is composed of four nested feedback loops (Fig. 2), acting on the brake pressures (p_L and p_R), the wheels' slip ratio (S_{xL} and S_{xR}), the aircraft heading (ψ) and the ground path (y). In particular, the heading control can be performed by using three commands: the rudder (δ_r), the nose-wheel steering (δ_s), and the differential brakes (T_{bL} and T_{bR}). The system operates in two modes:

- Normal mode, in which the brakes are commanded by the same slip ratio demand (S_{xi}) and are only used to decelerate the aircraft, while the directional control is (conventionally) performed by the rudder and the steering;
- Fail-Operative mode, in which, with failed steering (e.g. jammed), differential commands ($S_{xd\,i}$) are sent to the brakes, to compensate the failure and provide the aircraft with adequate directional stability.

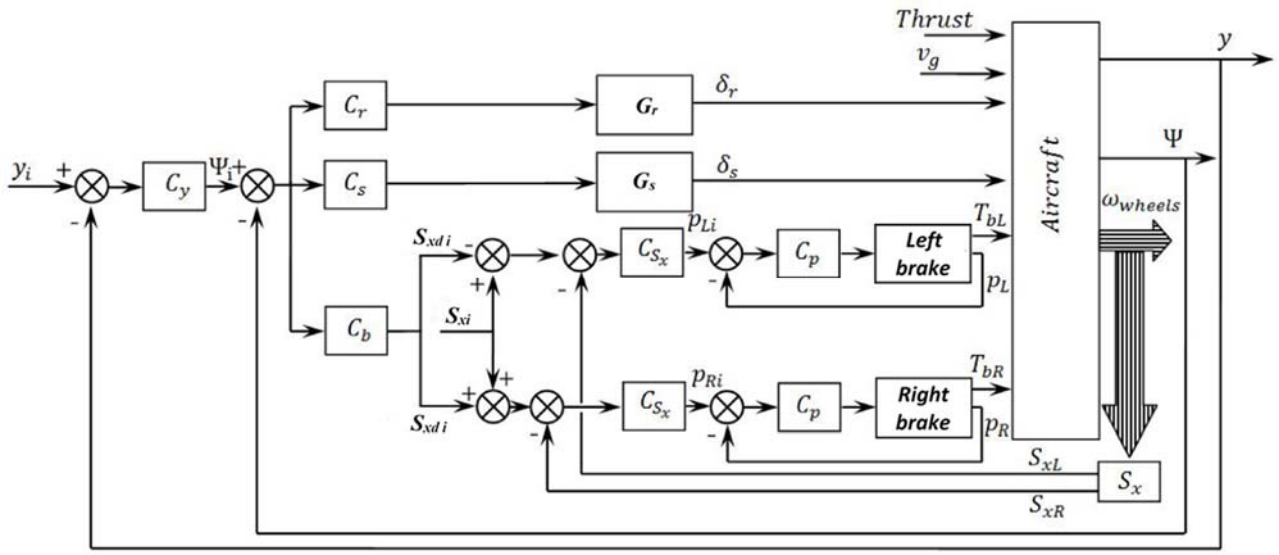

Fig. 2. Fault-tolerant control system of the aircraft runway dynamics: complete architecture.

3 System Modelling

3.1 Aircraft Runway Dynamics

The model of the aircraft runway dynamics is provided by Eq. (1), where the 6-degree-of-freedom momentum equations are written in a body-axes reference frame with the origin at the aircraft centre of gravity, the x-axis aligned with the fuselage longitudinal axis and oriented towards forebody, the z-axis vertically oriented to the ground and y-axis consequently.

$$\begin{cases} m_{ac}\left(\dot{\mathbf{V}}+\boldsymbol{\Omega}\times\mathbf{V}\right)=\mathbf{F}_a+\mathbf{F}_t+\mathbf{F}_{gN}+\mathbf{F}_{gL}+\mathbf{F}_{gR}+\mathbf{F}_W \\ [\mathbf{J}]\dot{\boldsymbol{\Omega}}+\boldsymbol{\Omega}\times[\mathbf{J}]\boldsymbol{\Omega}=\mathbf{M}_a+\mathbf{M}_t+\mathbf{a}_{gN}\times\mathbf{F}_{gN}+\mathbf{a}_{gL}\times\mathbf{F}_{gL}+\mathbf{a}_{gR}\times\mathbf{F}_{gR} \end{cases} \quad (1)$$

The weight force, and the aerodynamic forces and moments are given by Eqs. (2)-(4),

$$\mathbf{F}_W=[\mathbf{M}]_{E\to B}\begin{bmatrix}0 & 0 & m_{ac}g\end{bmatrix}^T \quad (2)$$

$$\mathbf{F}_a=[\mathbf{M}]_{W\to B}\begin{bmatrix}-C_D\\ C_Y\\ -C_L\end{bmatrix}\frac{\rho U^2 S}{2} \quad (3)$$

$$\mathbf{M}_a=[\mathbf{M}]_{W\to B}\begin{bmatrix}C_l b\\ C_m \bar{c}\\ C_n b\end{bmatrix}\frac{\rho U^2 S}{2} \quad (4)$$

where the coordinate transformation matrices from earth and wind reference frames to the body reference ($[\mathbf{M}]_{E\to B}$ and $[\mathbf{M}]_{W\to B}$ respectively) are defined in Eqs. (5)-(6). The Euler angles Φ, Θ and Ψ in Eq. (5) are related to the aircraft angular rates via Eq. (7).

$$[\mathbf{M}]_{E\to B}=\begin{bmatrix}\mathrm{c}\Theta\,\mathrm{c}\Psi & \mathrm{c}\Theta\,\mathrm{s}\Psi & -\mathrm{s}\Theta\\ \mathrm{s}\Phi\,\mathrm{s}\Theta\,\mathrm{c}\Psi-\mathrm{c}\Phi\mathrm{s}\Psi & \mathrm{s}\Phi\,\mathrm{s}\Theta\,\mathrm{s}\Psi+\mathrm{c}\Phi\,\mathrm{c}\Psi & \mathrm{c}\Theta\,\mathrm{s}\Phi\\ \mathrm{c}\Phi\,\mathrm{s}\Theta\,\mathrm{c}\Psi+\mathrm{s}\Phi\mathrm{s}\Psi & \mathrm{c}\Phi\,\mathrm{s}\Theta\,\mathrm{s}\Psi-\mathrm{s}\Phi\,\mathrm{c}\Psi & \mathrm{c}\Theta\,\mathrm{c}\Phi\end{bmatrix} \quad (5)$$

$$[\mathbf{M}]_{W\to B}=\begin{bmatrix}\mathrm{c}\alpha\,\mathrm{c}\beta & -\mathrm{c}\alpha\,\mathrm{s}\beta & -\mathrm{s}\alpha\\ \mathrm{s}\beta & \mathrm{c}\beta & 0\\ \mathrm{s}\alpha\mathrm{c}\beta & -\mathrm{s}\alpha\,\mathrm{s}\beta & \mathrm{c}\alpha\end{bmatrix} \quad (6)$$

$$\begin{bmatrix}\dot{\Phi}\\ \dot{\Theta}\\ \dot{\Psi}\end{bmatrix}=\begin{bmatrix}1 & \mathrm{s}\Phi\mathrm{t}\Theta & \mathrm{c}\Phi\mathrm{t}\Theta\\ 0 & \mathrm{c}\Phi & -\mathrm{s}\Phi\\ 0 & \mathrm{s}\Phi/\mathrm{c}\Theta & \mathrm{c}\Phi/\mathrm{c}\Theta\end{bmatrix}\boldsymbol{\Omega} \quad (7)$$

The aerodynamic coefficients appearing in Eqs. (3)-(4) are defined by Eqs. (8)-(9), while the force and the lever arm related to the j-th landing gear are provided by Eqs. (10)-(15).

$$\begin{cases} C_D=C_{D0}+\dfrac{C_L^2}{\pi\,AR\,e} \\ C_L=C_{L0}+C_{L\alpha}\alpha+C_{Lq}\hat{q} \\ C_Y=C_{Y\beta}\beta+C_{Y\delta_r}\delta_r \end{cases} \quad (8)$$

$$\begin{cases} C_l=C_{l\beta}\beta+C_{lp}\hat{p}+C_{lr}\hat{r}+C_{l\delta r}\delta_r \\ C_m=C_{m0}+C_{m\alpha}\alpha+C_{mq}\hat{q} \\ C_n=C_{n\beta}\beta+C_{np}\hat{p}+C_{nr}\hat{r}+C_{n\delta_r}\delta_r \end{cases} \quad (9)$$

$$\mathbf{F}_{gj}=[\mathbf{M}]_{E\to B}\mathbf{F}_{gj}|_E \quad (10)$$

$$\mathbf{F}_{gN}|_E=\begin{bmatrix}-F_{yN}\sin\delta_s\\ F_{yN}\cos\delta_s\\ F_{vN}\end{bmatrix} \quad (11)$$

$$\boldsymbol{F}_{gM}|_E = \begin{bmatrix} -F_{bM} \\ F_{yM} \\ F_{vM} \end{bmatrix} \quad where\ M = L, R \tag{12}$$

$$\mathbf{a}_{gN} = \begin{bmatrix} b_N & 0 & h_{GW} \end{bmatrix}^{\mathrm{T}} \tag{13}$$

$$\mathbf{a}_{gR} = \begin{bmatrix} -b_M & s_{GW} & h_{GW} \end{bmatrix}^{\mathrm{T}} \tag{14}$$

$$\mathbf{a}_{gL} = \begin{bmatrix} -b_M & -s_{GW} & h_{GW} \end{bmatrix}^{\mathrm{T}} \tag{15}$$

The model neglects thrust ($\mathbf{F}_t$) and the related moment ($\mathbf{M}_t$), while the tyre loads are based on the models provided in [19].

3.2 Servo-hydraulic brakes

The hydraulic actuation system of the aircraft brakes (depicted in the simplified sketch of Fig. 3) is simulated by modelling [20]:

- the three-way valve flow, Eqs (16)-(20);
- the valve spool dynamics, Eq. (21);
- the actuator dynamics, Eqs. (22)-(23);
- the disc brake release/compression, Eq. (24).

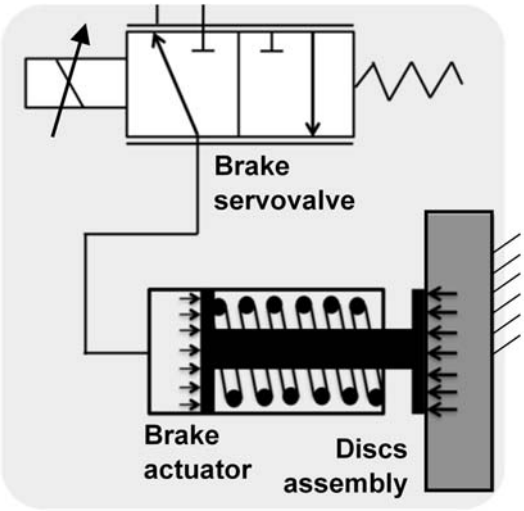

Fig. 3. Servo-hydraulic brake schematics.

$$q_{sj} = C_d \sqrt{\frac{2}{\rho_f}} A_{sj} \sqrt{P_s - P_{aj}} \tag{16}$$

$$q_{rj} = C_d \sqrt{\frac{2}{\rho_f}} A_{rj} \sqrt{P_{aj} - P_r} \tag{17}$$

$$q_{aj} = q_{sj} - q_{rj} \tag{18}$$

$$A_{rj} = \begin{cases} w(u - x_{vj}) & x_{vj} \le u \\ 0 & x_{vj} > u \end{cases} \tag{19}$$

$$A_{sj} = \begin{cases} 0 & x_{vj} < -u \\ w(x_{vj} + u) & x_{vj} \ge -u \end{cases} \tag{20}$$

$$\ddot{x}_{vj} = -2\zeta_v \omega_v \dot{x}_{vj} - {\omega_v}^2 x_{vj} + {\omega_v}^2 x_{vj\ dem} \tag{21}$$

$$\dot{P}_{aj} = \frac{\beta_f}{A_{af} x_{afj}} \left(q_{aj} - A_{af} \dot{x}_{afj} \right) \tag{22}$$

$$m_{af} \ddot{x}_{afj} = P_{aj} A_{af} - K_p x_{dj} - K_{af} x_{afj} - C_{af} \dot{x}_{afj} \tag{23}$$

$$x_{dj} = \begin{cases} x_{afj} - x_{aZTP} & x_{afj} \ge x_{aZTP} \\ 0 & x_{afj} < x_{aZTP} \end{cases} \tag{24}$$

3.3 Nose-wheel steering

Concerning the nose-wheel steering, the simulator also includes a detailed model of a position-controlled EMA (Fig. 4), composed by permanent magnet synchronous motor, epicyclical gearbox, emergency clutch, digital control electronics and sensors (resolver, current sensors and RVDT). Nevertheless, the EMA model description is not reported, since the attention of the study is focused on the aircraft behaviour with a jammed nose-wheel steering, a situation that is simulated by simply imposing a fixed position of the nose-wheel angle with respect to fuselage during the runway dynamics.

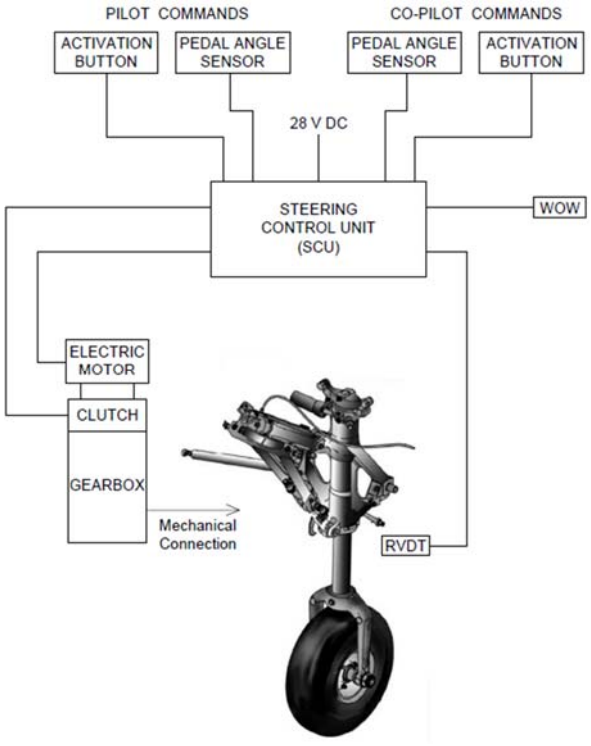

Fig. 4. Nose-wheel steering EMA schematics.

4 Simulation study

4.1 Directional control design

In the proposed system architecture, the directional control (i.e. heading tracking) can be performed by three commands: the conventional rudder and steering, plus the differential brakes. For each command axis, the regulator has been obtained via model-inversion technique, by imposing the same heading tracking dynamic performance (45° phase delay at 0.5 Hz, 3 dB maximum amplitude) [21].
Figure 5 shows the results of this design, in terms of heading tracking frequency responses. It can be noted that the closed-loop heading dynamics behaves similarly up to 1 Hz for all directional commands.

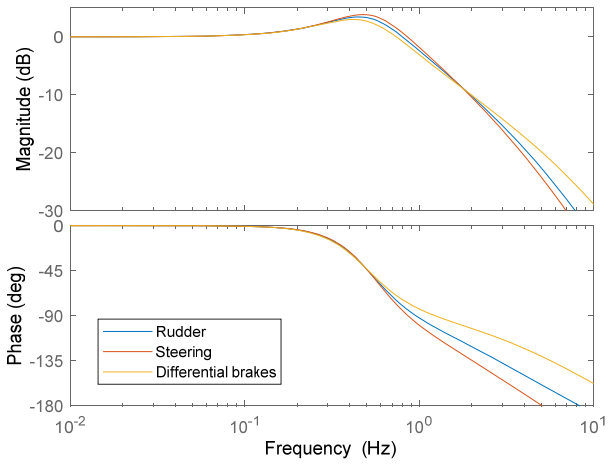

Fig. 5. Heading tracking frequency responses.

4.2 Simulation campaign

The effectiveness of the developed fault-tolerant control system has been verified with an extensive test campaign, by simulating the runway dynamics from the aircraft touchdown (at 50 m/s longitudinal speed) to the beginning of the taxiing phase (i.e. when speed is lower than 5 m/s), in case of nose-wheel steering jamming with severe crosswind conditions.
In particular, the onset of the lateral gust is simulated as defined in [22], Eq. (25),

$$v_g(x) = \frac{v_{de}}{2}\left[1-\cos\left(\frac{2\pi x}{25\bar{c}}\right)\right] \qquad (25)$$

and the gust intensity is held at the maximum value through all the runway dynamics.
In Eq. (25), v_{de} is the derived gust speed, $\bar{c}$ is the mean aerodynamic chord of the aircraft wing, x is the distance penetrated inside the gust, v_g is the gust speed at generic position inside the gust. In the test campaign, v_{de} has been set to 15 m/s.
Table 1 reports a set of simulation test cases, selected for highlighting and characterizing, at different runway conditions, the effects of jamming detection latency on the aircraft directional stability.

Test case	Differential brakes activation [Y/N]	Activation latency [msec]	Runway condition [dry/wet]
1	N	n.d.	wet
2	Y	0	wet
3	Y	500	wet
4	Y	500	dry

Table 1. Simulation test cases.

Figure 6 points out that, in case of nose-wheel steering jamming, the rudder is not capable to assure the directional stability if severe crosswinds are encountered. On the other hand, the activation of the differential brakes demonstrate to be very effective, with maxima lateral displacements ranging from 1 m (with dry runway) to 2.5 m (with wet runway).

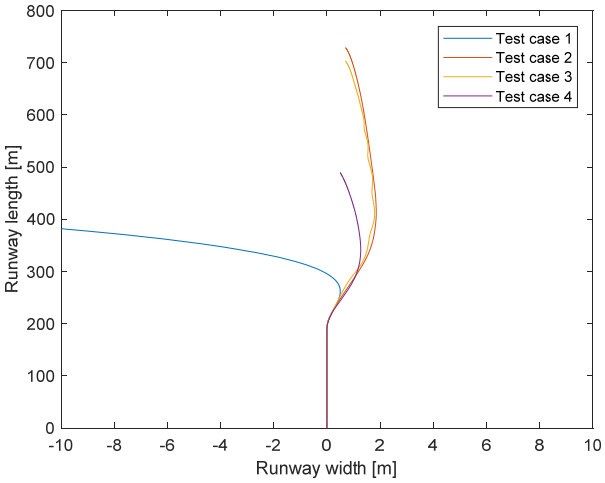

Fig. 6. Ground path response.

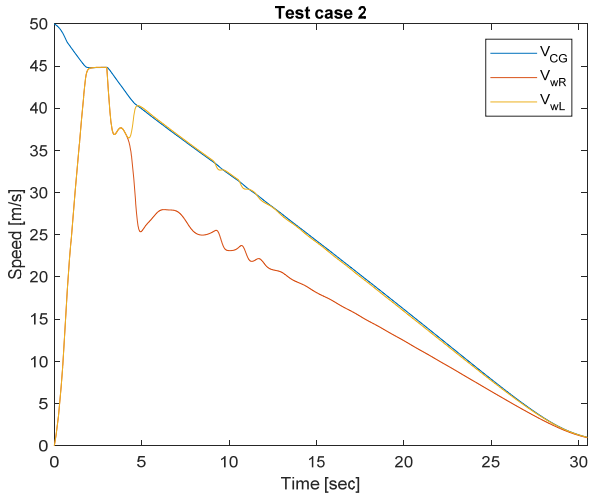

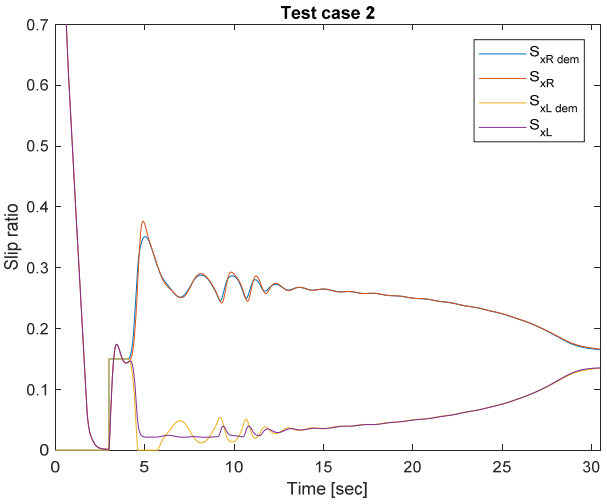

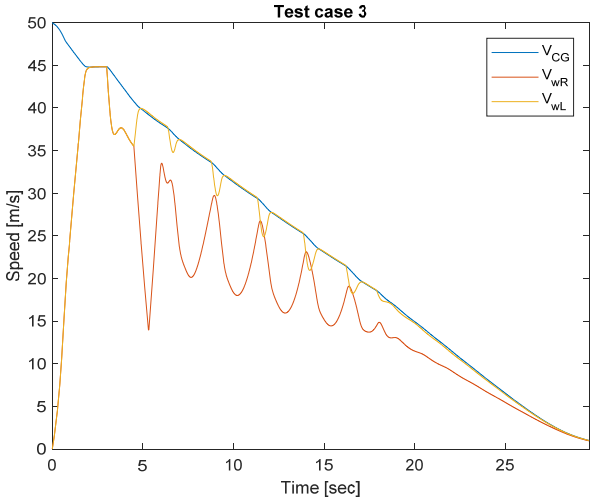

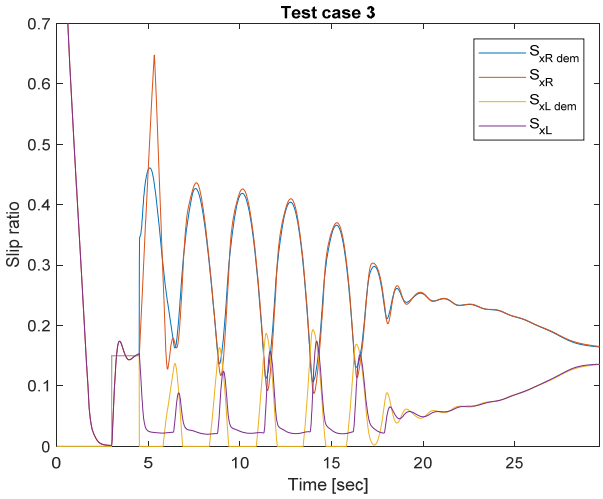

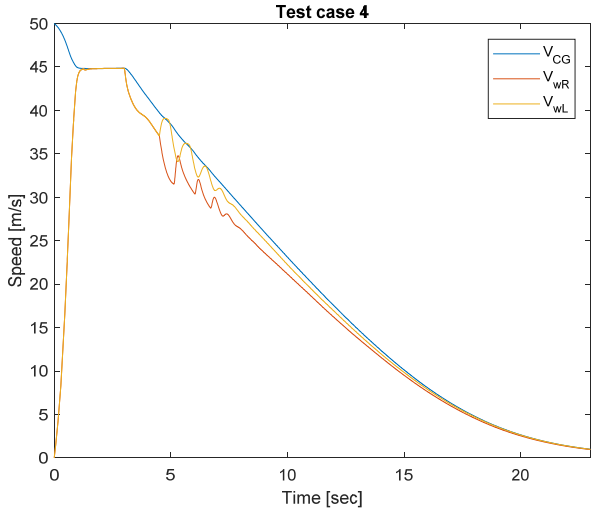

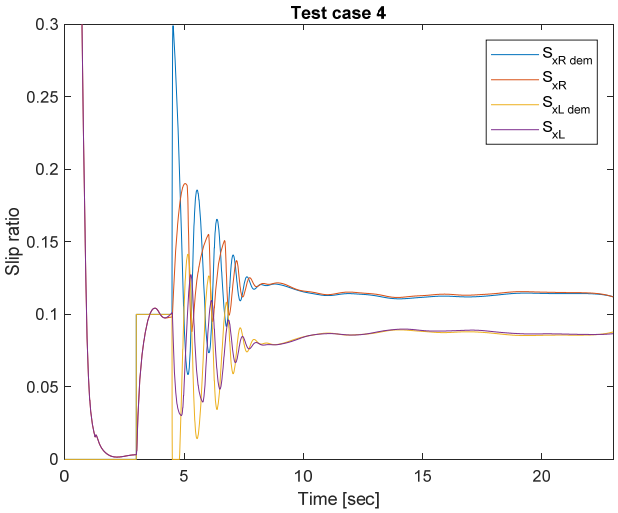

Fig. 7. Aircraft speed and wheels' speed.

Fig. 8. Wheels' slip ratios.

Figure 7, Figure 8 and Figure 9 clearly show the effects of the activation latency of the differential brakes. If the nose-wheel steering jamming is immediately detected (Test case 2), the fault-tolerant control system exhibits very good results even with wet runway.

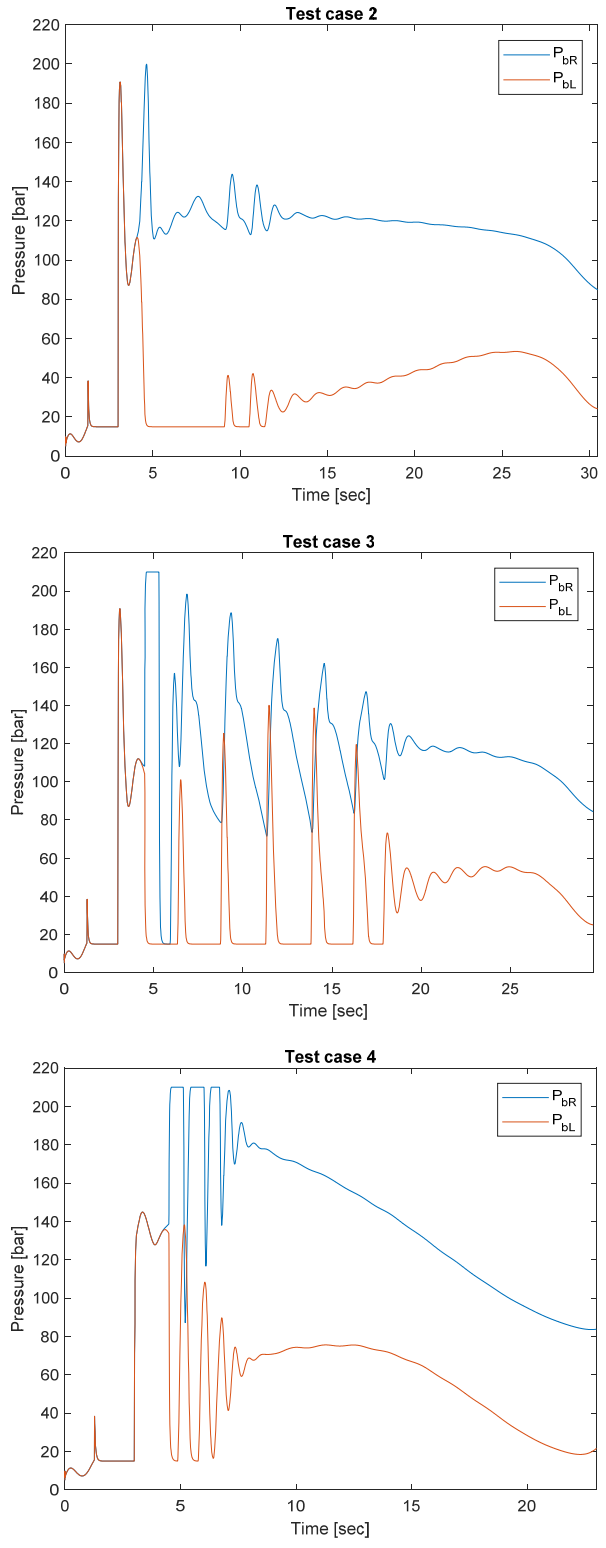

Fig. 9. Brakes' pressure.

On the other hand, if the activation occurs 500 msec after the jamming occurrence, undesired oscillations are generated, especially in wet runway conditions (Test case 3), in which the wheel of the right main landing gear tends to block. The phenomenon is caused by the delayed and amplified slip ratio demand for the directional control as well as by the intrinsic increase of the vertical load on the wheel that is opposite to the crosswind direction. Similar considerations can be made with reference to the pressures in the brakes, with additional concerns about possible cavitation problems due to the repeated and abrupt oscillations between supply and return pressure levels.

Conclusions

The work points out that the use of fault-tolerant control system merging servo-hydraulic and electro-mechanical technologies can represent a good solution for applying the "more electric" concept in safety-critical aerospace applications. In the proposed case study, the runway directional control of a light business jet aircraft is performed by a fault-tolerant architecture, with conventional rudder/steering combined commands, plus the servo-hydraulic differential brakes in stand-by. Simulations highlight that, if the nose-wheel steering EMA jams, and the fault is promptly detected by activating the differential brakes, the system exhibits very good directional stability results in all runway conditions. However, a special attention must be paid to the design of health-monitoring systems, because even small activation latencies (500 msec) can cause undesired and dangerous oscillations of braking wheel speeds and brake pressures, especially in wet runway conditions.

References

[1] Botten S-L, Whitley C-R, and King A-D. Flight control actuation technology for next generation all-electric aircraft. *Technology Review Journal*, pp. 55-68, 2000.

[2] Davis M-A. High performance electromechanical servoactuation using brushless DC motors (Moog Technical Bulletin 150). *Proceedings of the MOTOR-CON '84 Conference*, Atlantic City, NJ, USA, April 1984.

[3] Di Rito G, Galatolo R and Denti E. Object-oriented modelling of flight control actuation systems for power absorption assessment. *Proceedings of the 27th Congress of the International Council of Aeronautical Sciences (ICAS)*, Nice, France, September 2010.

[4] Di Rito G, Galatolo R and Schettini F. Experimental and simulation study of the dynamics of an electro-

mechanical landing gear actuator. *Proceedings of the 30th Congress of the International Council of the Aeronautical Sciences (ICAS)*, Daejeon, South Korea, September 2016.

[5] Balaban E, Bansal P, Stoelting P, Saxena A, Goebel K-F and Curran S. A diagnostic approach for electro-mechanical actuators in aerospace systems. *Proceedings of the 2009 IEEE Aerospace Conference*, Big Sky, MT, USA, March 2009.

[6] Mohamed A-A, Balaban E and Spangenberg H. Fault detection and classification for flight control electromechanical actuators. *Proceedings of the 2016 IEEE Aerospace Conference*, Big Sky, MT, USA, March 2016.

[7] Ossmann D and Van der Linden F-L-J. Advanced sensor fault detection and isolation for electro-mechanical flight actuators. *Proceedings of the NASA/ESA Conference on Adaptive Hardware and Systems*, Montreal, Canada, 2015, pp. 1-8.

[8] Arriola D and Thielecke F. Design of fault-tolerant control functions for a primary flight control system with electromechanical actuators, *Proceedings of the International Conference Autotestcon 2015*, , National Harbour, Maryland, USA, 2015, pp. 393-402.

[9] Di Rito G, Schettini F and Galatolo R. Self-monitoring electro-mechanical actuator for medium altitude long endurance unmanned aerial vehicle flight controls. *Advances in Mechanical Engineering – Special Issue on Reliability for Aerospace Systems: Methods and Applications*, Vol. 8, N. 5, pp. 1–11, 2016.

[10] Di Rito G and Schettini F. Health monitoring of electromechanical flight actuators via position-tracking predictive models. *Advances in mechanical engineering*, Vol. 10, N. 4, pp. 1–12, 2018.

[11] Fawaz Y-A. Fundamental design concepts in multi-lane smart electromechanical actuators. *Smart Materials and Structures*, Vol. 14, pp. 1227-1238, 2005.

[12] Garcia A, Cusidò I, Rosero J-A, Ortega J-A and Romeral L. Reliable electro-mechanical actuators in aircraft. *IEEE A&E Systems Magazine*, pp. 19-25, 2008.

[13] Rottach M, Gerada C and Wheeler P-W. Design optimisation of a fault-tolerant PM motor drive for an aerospace actuation application. *Proceedings of 7th IET International Conference on Power Electronics, Machines and Drives*, Manchester, UK, 2014.

[14] Smith M-J Byington C-S, Watson M-J, Bharadwaj S, Swerdon G, Goebel K and Balaban E. Experimental and analytical development of health management for electro-mechanical actuators. *Proceedings of the 2009 IEEE Aerospace conference*, Big Sky, MT, USA, March 2009.

[15] Di Rito G and Galatolo R. Experimental assessment of the dynamic stiffness of a fault-tolerant fly-by-wire hydraulic actuator. *Proceedings of the Institution of Mechanical Engineers - Part G: Journal of Aerospace Engineering*, Vol. 226, N. 6, pp. 679-690, 2012.

[16] Di Rito G, Schettini F and Galatolo R. Model-based prognostic health-management algorithms for the freeplay identification in electromechanical flight control actuators, *Proceedings of the 5th IEEE International Workshop on Metrology for Aerospace*, Roma, Italia, June 2018, pp. 340-345.

[17] Soderman P-T and Aiken T-N. Full-scale wind-tunnel test of a small unpowered jet aircraft with a T-tail. *NASA TN D-6573, Ames Research Center and US Army Air Mobility R&D Laboratory*, Washington DC, USA, November 1971.

[18] www.cleansky.eu/small-air-transport

[19] Pacejka H-B and Bakker E. The magic formula tyre model. *Tyre Models for Vehicle Dynamics Analysis*, Vol. 21, 1991.

[20] Tunay I, Rodin E Y and Beck A A. Modeling and robust control design for aircraft brake hydraulics. *IEEE Transactions on Control Systems Technology*, Vol. 9, pp. 319–329, 2001.

[21] McGee T-G and Hedrick J-K. Path planning and control for multiple point surveillance by an unmanned aircraft in wind. *Proceedings of the 2006 American Control Conference*, Minneapolis, MN, USA, June 2006, pp. 4261-4266.

[22] European Aviation Safety Agency, Certification specifications and acceptable means of compliance for normal, utility, aerobatic, and commuter category aeroplanes, CS-23, Amendment 4, 15 July 2015.

Copyright Statement

Contact Author Email Address

g.dirito@dia.unipi.it

Appendix

Notations

Symbol	Definition	Unit
α	Angle-of-attack	rad
β	Angle-of-sideslip	rad
β_f	Fluid bulk modulus	rad
δ_r	Rudder deflection	rad
δ_s	Nose-wheel steering angle	rad
ρ	Air density	kg/m^3
ρ_f	Fluid density	kg/m^3
Φ, Θ, Ψ	Euler angles	rad
p	Roll rate	rad/s
q	Pitch rate	rad/s
q_{aj}	Valve flow rate of the j-th brake (cylinder line)	m^3/s
q_{rj}	Valve flow rate of the j-th brake (return line)	m^3/s
q_{sj}	Valve flow rate of the j-th brake (supply line)	m^3/s
r	Yaw rate	rad/s
u	Valve underlap	m
v_{de}	Derived gust speed	m/s
v_g	Gust speed	m/s
$x_{af\,j}$	Actuator displacement of the j-th brake	m
x_{aZTP}	Actuator displacement at zero-torque pressure (ZTP)	m
$x_{d\,j}$	Disc assembly compression of the j-th brake	m
x_{vj}	Valve opening of the j-th brake	m
$x_{vj\,dem}$	Valve opening demand of the j-th brake	m
A_{af}	Cylinder area	m^2
A_{rj}	Orifice area of the j-th brake (return line)	m^2
A_{sj}	Orifice area of the j-th brake (supply line)	m^2
C_d	Orifice discharge coefficient	--
$[\boldsymbol{J}]$	Aircraft matrix of inertia	[kg m^2]
P_{aj}	Cylinder pressure of the j-th brake	m^3/s
S_x	Wheel slip ratio	--

Reference aircraft data

Symbol	Definition	Value	Unit
AR	Wing aspect ratio	5	--
e	Oswald coefficient	0.8	--
m_{ac}	Aircraft mass	4536	kg
b	Wing span	10.4	m
S	Wing reference area	21.5	m^2
c	Mean aerodynamic chord	2.14	m
l_{gear}	Longitudinal distance between landing gears	4.93	m
b_M	Longitudinal distance between main landing gears and aircraft C.G.	0.74	m
b_N	Longitudinal distance between nose landing gears and aircraft C.G.	4.19	m
s_{GW}	Lateral distance between main landing gears and aircraft C.G.	1.32	m
h_{GW}	Vertical distance of aircraft C.G. from ground	1	m
J_x	Moment of inertia around roll axis	35926	kg m^2
J_y	Moment of inertia around pitch axis	33940	kg m^2
J_z	Moment of inertia around yaw axis	67085	kg m^2
J_{xz}	Moment of inertia around roll/yaw axis	3418	kg m^2
C_{D0}	Drag coefficient	0.0255	--
$C_{Y\beta}$	Lateral force slope coefficient wrt sideslip angle	-0.646	1/rad
$C_{Y\delta r}$	Lateral force slope coefficient wrt rudder deflection	0.157	1/rad
C_{L0}	Lift coefficient at zero angle-of-attack	0.11	--
$C_{L\alpha}$	Lift slope coefficient wrt angle-of-attack	5.65	1/rad
C_{Lq}	Lift slope coefficient wrt pitch rate	0.09	s/rad
$C_{l\beta}$	Roll moment slope coefficient wrt sideslip angle	-0.092	1/rad
C_{lp}	Roll moment slope coefficient wrt roll rate	-0.082	s/rad
C_{lr}	Roll moment slope coefficient wrt yaw rate	0.00015	s/rad
$C_{l\delta r}$	Roll moment slope coefficient wrt rudder deflection	0.021	1/rad
C_{m0}	Pitch moment coefficient	0.038	
$C_{m\alpha}$	Pitch moment slope coefficient wrt angle-of-attack	-1.217	1/rad
C_{mq}	Pitch moment slope coefficient wrt pitch rate	-0.67	s/rad
$C_{n\beta}$	Yaw moment slope coefficient wrt sideslip angle	0.143	1/rad
C_{np}	Yaw moment slope coefficient wrt roll rate	0.00015	s/rad
C_{nr}	Yaw moment slope coefficient wrt yaw rate	-0.013	s/rad
$C_{n\delta r}$	Yaw moment slope coefficient wrt rudder deflection	-0.07	1/rad